Modelling of hydraulic fracture propagation in inhomogeneous poroelastic medium

A N Baykin[1] **and S V Golovin**[1,2]

[1] Novosibirsk State University, Novosibirsk, Russia
[2] Lavrentyev Institute of Hydrodynamics SB RAS, Novosibirsk, Russia

E-mail: alexey.baykin@gmail.com, svgolovin@gmail.com

Abstract. In the paper a model for description of a hydraulic fracture propagation in inhomogeneous poroelastic medium is proposed. Among advantages of the presented numerical algorithm, there are incorporation of the near-tip analysis into the general computational scheme, account for the rock failure criterion on the base of the cohesive zone model, possibility for analysis of fracture propagation in inhomogeneous reservoirs. The numerical convergence of the algorithm is verified and the agreement of our numerical results with known solutions is established. The influence of the inhomogeneity of the reservoir permeability to the fracture time evolution is also demonstrated.

1. Introduction

Hydraulic fracturing is an important part of modern technologies for intensification of hydrocarbon production. The propagation of the hydraulic fracture is stimulated by the pumping of viscous fluid which creates pressure on fracture's walls high enough to overcome the rock closure stresses and cause the rock failure. Process of the hydraulic fracture growth is governed by several factors: flow of viscous fluid in a narrow fracture's gap, elastic reaction of the fracture's walls, filtration of fluid from the fracture to the reservoir, rock failure and advance of the fracture tip. Description of the hydraulic fracture dynamics is a complicated problem that is rarely solved in its most general formulation. Recent progress in the mathematical modelling of hydraulic fracture dynamics is described in review papers [1, 2].

In the present work the poroelastic model proposed in [3] is extended to the case of propagating fractures. The model allows determination of the porous pressure and the rock deformation coupled with the fracture disclosure and the pressure of the fracturing fluid. The material of the formation is observed as an inhomogeneous permeable medium governed by the Biot poroelasticity equations [4, 5]. The advantages of this approach in comparison with the classical approaches based on the KGD and PKN models (see [1, 2]) are the correct account for the interaction of the pore fluid with the fracturing fluid, finiteness of fluid pressure in the fracture's tip, readiness for modelling of reservoirs with inhomogeneous physical properties under non-uniform closure stresses.

The numerical solution of the problem was carried out by the finite element method with the use of a modification of the algorithm proposed in [3]. The advantages of this algorithm is lack of necessity for explicit track of the fracture's tip and corresponding remeshing, which is typical for contact problems of this type. The numerical convergence of the algorithm and possibility

for computation of problems of the scale required for the engineering practice with a satisfactory accuracy is demonstrated. Also we present some results demonstrating the dependence of the fracture geometry and propagation behavior on the inhomogeneity of reservoir permeability.

2. Mathematical formulation of the problem

In this paper we make use of the model proposed in [3]. The mathematical problem is formulated in the following way. Let us consider a vertical planar fracture of fixed height H, propagating along the x axis (see Figure 1). Oz axis is directed upwards relative to the Oxy-plane. The fracture is opening along y direction due to the pressure generated by the fluid flow inside the fracture. Following [3] we suppose that fracture aperture is constant along z-coordinate and vertical deformations are negligible. This implies, that we can limit ourselves to the plane strain approximation observing only the central cross-section $z = 0$ of the fracture.

The poroelastic medium is characterized by its porosity ϕ and permeability $k_r(\mathbf{x})$, with the solid phase displacement $\mathbf{u}(t, \mathbf{x})$, and the pore pressure $p(t, \mathbf{x})$. Pores are saturated by a single-phase Newtonian fluid with the effective viscosity η_r. The linear Darcy's law for the fluid velocity $\mathbf{q} = -(k_r/\eta_r)\nabla p$ is employed. It is supposed that the fluid filtrating from the fracture to the reservoir has the same viscosity as the pore fluid. However, the fluid injected into the fracture has different viscosity η_f. It corresponds to the normal situation in hydraulic fracturing when the fracturing fluid is a high-viscous gel and only its low-viscous base fluid is filtrated into the reservoir.

For generality, the reservoir is initially subjected to a prestress with the stress tensor $\boldsymbol{\tau}_0(x, y)$. Hereafter, only planar fractures propagating along Ox axis are observed, therefore, the tensor $\boldsymbol{\tau}_0$ satisfies the symmetry conditions relative to this axis.

The governing equation of the quasi-static poroelasticity model is the following:

$$\begin{aligned} &\operatorname{div} \boldsymbol{\tau} = 0, \quad \boldsymbol{\tau} = \boldsymbol{\tau}_0 + \lambda \operatorname{div} \mathbf{u}\, \mathrm{I} + 2\mu\, \mathcal{E}(\mathbf{u}) - \alpha p\, \mathrm{I}, \\ &S_\varepsilon \frac{\partial p}{\partial t} = \operatorname{div}\Big(\frac{k_r}{\eta_r}\nabla p - \alpha \frac{\partial \mathbf{u}}{\partial t}\Big). \end{aligned} \tag{1}$$

Here $\mathcal{E}(\mathbf{u})$ is the Cauchy's strain tensor $2\mathcal{E}(\mathbf{u})_{ij} = \partial u_i/\partial x_j + \partial u_j/\partial x_i$ $(i, j = 1, 2)$, α is the Biot coefficient, $\lambda(\mathbf{x})$ and $\mu(\mathbf{x})$ are elasticity moduli, I is the identity tensor. The storativity S_ε reflects the dependence of the Lagrangian porosity ϕ on $\epsilon = \operatorname{tr} \mathcal{E}$ and p as in [6]:

$$\frac{\partial \phi}{\partial t} = \alpha \frac{\partial \epsilon}{\partial t} + S_\varepsilon \frac{\partial p}{\partial t}, \quad S_\varepsilon = \frac{(\phi_0 - \alpha)(1 - \alpha)}{K}, \tag{2}$$

where $K = \lambda + \dfrac{2\mu}{3}$ is the bulk modulus, ϕ_0 is the initial porosity. Due to the plane strain approximation, the solid phase displacement vector $\mathbf{u} = (u_1, u_2) = (u, v)$ is two-dimensional, all vector operations are also taken in 2D space of independent variables $(x_1, x_2) = (x, y)$.

Symmetry of the problem with respect to Ox-axis makes it possible solving equations (1) in domain $\Omega = \{(x, y) : |x| \le R, 0 \le y \le R\}$ as shown in Figure 2. Over the outer boundary $\Gamma_R : \ |\mathbf{x}|_\infty = R$, the confining far-field stress $\boldsymbol{\sigma}_\infty$ is applied and the constant pore pressure $p = p_\infty$ is prescribed:

$$\Gamma_R : \quad p = p_\infty, \quad \boldsymbol{\tau}\langle \mathbf{n} \rangle = \boldsymbol{\sigma}_\infty, \quad (\boldsymbol{\tau}\langle \mathbf{n} \rangle)_i = \tau_{ij} n_j. \tag{3}$$

Henceforth, $\mathbf{n}$ and $\mathbf{s}$ denote the outer normal and tangential unit vectors to the boundary of the domain Ω; the summation over the repeating index is implied. We restrict ourselves to the case with $\boldsymbol{\sigma}_\infty = -\sigma_\infty \mathbf{e}_2$, where σ_∞ is a scalar function. Moreover, it is assumed that the presstress $\boldsymbol{\tau}_0$ satisfies the same boundary condition: $\boldsymbol{\tau}_0\langle \mathbf{n} \rangle|_{\Gamma_R} = \boldsymbol{\sigma}_\infty$.

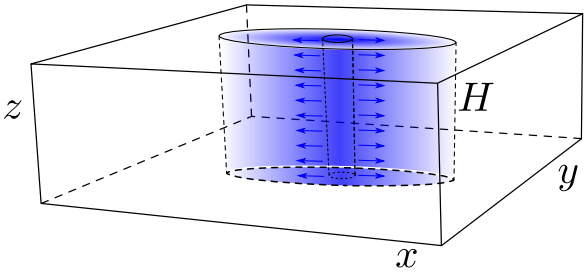

Figure 1. Planar vertical hydraulic fracture in a poroelastic medium

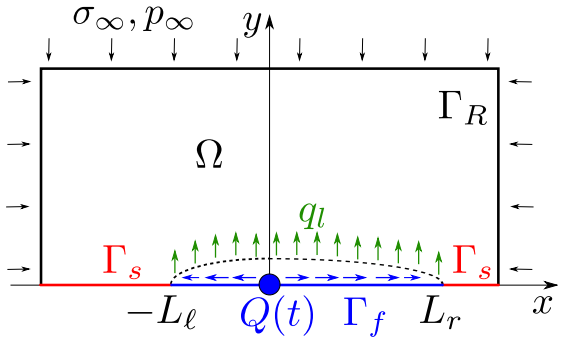

Figure 2. The horizontal cross-section of the fracture by plane $z = 0$

The line $y = 0$ is divided into the part $\Gamma_f = \{-L_\ell(t) \leqslant x \leqslant L_r(t),\ y = 0\}$ occupied by the fracture, and the remaining part $\Gamma_s = \{-R < x < -L_\ell(t),\ y = 0\} \bigcup \{L_r(t) < x < R,\ y = 0\}$. Outside the fracture on Γ_s the symmetry conditions (see [3]) are satisfied:

$$\Gamma_s: \quad \frac{\partial u}{\partial y} = 0, \quad v = 0, \quad \frac{\partial p}{\partial y} = 0. \tag{4}$$

With $p_f(t, x)$ standing for the fluid pressure inside the fracture, the force balance over the fractures walls yields

$$\Gamma_f: \quad p = p_f, \quad \mathbf{n} \cdot \boldsymbol{\tau} \langle \mathbf{n} \rangle = -p_f + \sigma_{coh}, \quad \mathbf{s} \cdot \boldsymbol{\tau} \langle \mathbf{n} \rangle = 0. \tag{5}$$

Here the tangential stress due to the fluid friction on the fractures walls in comparison with the normal stress is neglected.

In order to account for the rock failure during fracturing, the cohesive zone model is adopted as a fracture propagation criterion. Such an approach was initially proposed by Barenblatt [7] and Dugdale [8], where they postulated the existence of cohesive forces σ_{coh} (see Figure 3), which act in the zone of micro-cracking and plastic deformations in the vicinity of the fracture tips and prevent opening of the fracture. On the computational side, presence of cohesive forces removes the stress singularity at the fracture tip inherent to the Linear Elastic Fracture Mechanics (LEFM) by making the fracture aperture smoothly vanishing towards the tip.

We use the following traction/separation bi-linear law [9] to reflect the dependence of σ_{coh} on the half of the fracture aperture w as shown in Figure 4:

$$\sigma_{coh}(w) = \begin{cases} \sigma_c \dfrac{w}{w_m}, & 0 \leqslant w \leqslant w_m, \\ \sigma_c \left(\dfrac{w_c - w}{w_c - w_m} \right), & w_m \leqslant w \leqslant w_c, \\ 0, & w \geqslant w_c. \end{cases} \tag{6}$$

The cohesive forces reach their maximum value near the fracture tip. The region of the softening behaviour is limited by w_c. It is calculated from the considerations that the release of energy during the creation of the new fracture surface is equal to the work of the cohesive forces on the fracture opening. Hence,

$$G_c = \sigma_c \, w_c, \tag{7}$$

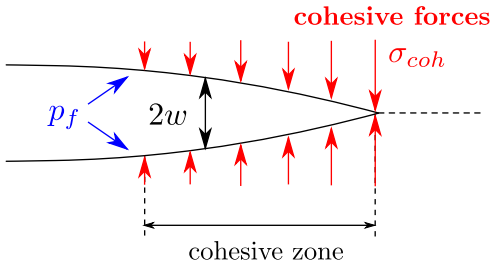

Figure 3. Cohesive zone near the fracture tip

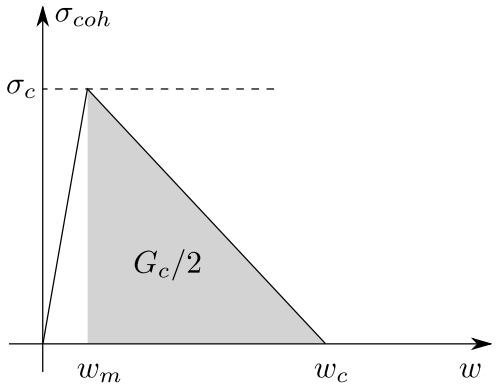

Figure 4. Bi-linear traction/separation law

where G_c is the energy release rate from the Griffiths's theory of brittle fractures [10], σ_c is the critical cohesive stress value. The elastic region of cohesive forces is small, $w_m = 2.5 \times 10^{-4} w_c$. It is required to regularize the cohesive energy near $w = 0$ [11].

If the cohesive zone is small relative to the fracture length, the connection with the fracture toughness K_{Ic} from LEFM is given by the Irvin's formula [12]:

$$K_{Ic} = \sqrt{G_c \frac{E}{1-\nu^2}}, \tag{8}$$

where E is the Young's modulus and ν is the Poisson's ratio.

The fluid flow in the fracture is governed by the mass conservation law complemented with the Poiseuille formula:

$$\frac{\partial w}{\partial t} + \frac{\partial (wq)}{\partial x} = -q_l, \quad w \equiv v|_{y=0}, \quad q = -\frac{(2w)^2}{12\eta_f}\frac{\partial p_f}{\partial x}. \tag{9}$$

Here q is the fluid velocity in x-direction. No fluid lag is assumed at the fracture tip.

The leak-off velocity q_l is given by the Darcy law in the reservoir as

$$q_l = -\left.\frac{k_r}{\eta_r}\frac{\partial p}{\partial y}\right|_{y=0}. \tag{10}$$

The resulting equation governing the flow inside the fracture reads

$$\frac{\partial w}{\partial t} = \frac{\partial}{\partial x}\left(\frac{w^3}{3\eta_f}\frac{\partial p_f}{\partial x}\right) + \left.\frac{k_r}{\eta_r}\frac{\partial p}{\partial y}\right|_{y=0}. \tag{11}$$

The flow rate (per unit height) injected into the fracture upper half-plane is calculated as

$$Q(t) = \frac{Q_v(t)}{2H} = -\left.\frac{w^3}{3\eta_f}\frac{\partial p_f}{\partial x}\right|_{x=0+} + \left.\frac{w^3}{3\eta_f}\frac{\partial p_f}{\partial x}\right|_{x=0-}, \tag{12}$$

where the division by 2 shows that the total flow rate is equally distributed between the symmetric fracture parts, and $Q_v(t)$ denotes the volumetric flow rate injected into the wellbore.

Equation (11) is often referred to as the lubrication theory equation [1]. Note that, due to the right-hand side of (10), equation (11) represents a boundary condition for equations of the main model (1). The leak-off rate q_l arises here naturally in the course of the problems

solution, which differentiates the model favourably from the usual artificial approximations like the Carters formula or other similar expressions [13].

In order to close the model it is supplemented with the initial data at some moment t^0:

$$\mathbf{u}|_{t=t^0} = \mathbf{u}^0(x,y), \quad p|_{t=t^0} = p^0(x,y), \quad L_i|_{t=t^0} = L_i^0,\ i = \ell, r. \tag{13}$$

For computational reasons, it is convenient to homogenise the conditions over the outer boundary Γ_R. It can be done by considering stresses inside the reservoir relative to the prestress state $\boldsymbol{\tau}_0$, and taking p_∞ as a reference pressure. Similar to [3] the following new sought functions are introduced:

$$\tilde{\mathbf{u}} = \mathbf{u} - \varkappa \mathbf{x}, \quad \varkappa = \frac{\alpha p_\infty}{2(\lambda+\mu)}, \quad \tilde{\boldsymbol{\tau}} = \boldsymbol{\tau} - \boldsymbol{\tau}_0, \quad \tilde{p} = p - p_\infty. \tag{14}$$

Substituting (14) into equations (1) and taking into account boundary conditions (3), (4), (5), (11), (12), we obtain the following problem

$$\Omega: \quad \operatorname{div}\tilde{\boldsymbol{\tau}} = -\operatorname{div}\boldsymbol{\tau}_0, \quad \tilde{\boldsymbol{\tau}} = \lambda \operatorname{div}\tilde{\mathbf{u}}\,\mathrm{I} + 2\mu\,\mathcal{E}(\tilde{\mathbf{u}}) - \alpha\tilde{p}\,\mathrm{I}, \tag{15}$$

$$\Omega: \quad S_\varepsilon \frac{\partial \tilde{p}}{\partial t} = \operatorname{div}\Big(\frac{k_r}{\eta_r}\nabla\tilde{p} - \alpha\frac{\partial \tilde{\mathbf{u}}}{\partial t}\Big), \tag{16}$$

$$\Gamma_R: \quad \tilde{p} = 0, \quad \tilde{\boldsymbol{\tau}}\langle\mathbf{n}\rangle = 0, \tag{17}$$

$$\Gamma_s: \quad \tilde{u_y} = 0, \quad \tilde{v} = 0, \quad \tilde{p_y} = 0, \tag{18}$$

$$\Gamma_f: \quad \mathbf{n}\cdot\tilde{\boldsymbol{\tau}}\langle\mathbf{n}\rangle = -(\tilde{p}+p_\infty) - \mathbf{n}\cdot\boldsymbol{\tau}_0\langle\mathbf{n}\rangle + \sigma_{coh}, \quad \mathbf{s}\cdot\tilde{\boldsymbol{\tau}}\langle\mathbf{n}\rangle = 0, \tag{19}$$

$$\Gamma_f: \quad \frac{\partial\tilde{v}}{\partial t} = \frac{\partial}{\partial x}\left(\frac{\tilde{v}^3}{3\eta_f}\frac{\partial\tilde{p}}{\partial x}\right) + \frac{k_r}{\eta_r}\frac{\partial\tilde{p}}{\partial y}; \quad -\frac{\tilde{v}^3}{3\eta_f}\frac{\partial\tilde{p}}{\partial x}\Big|_{y=0,x=0+} + \frac{\tilde{v}^3}{3\eta_f}\frac{\partial\tilde{p}}{\partial x}\Big|_{y=0,x=0-} = Q(t). \tag{20}$$

In what follows, we work with the new sought functions skipping the tilde for simplicity of notations.

3. Numerical algorithm

In this Section the numerical method to solve the problem stated in Section 2 is provided. To accomplish this, firstly, we write the variational formulation of the problem. Following [3] let us choose a smooth vector-function $\boldsymbol{\psi} = \big(\psi_1(x,y), \psi_2(x,y)\big)$ and a smooth scalar function $\varphi(x,y)$ such that

$$\psi_2|_{\Gamma_s} = 0, \quad \varphi|_{\Gamma_R} = 0. \tag{21}$$

Then, we multiply equations (15) and (16) by $\boldsymbol{\psi}$ and φ, respectively, and integrate over Ω. Taking into account the boundary conditions (17)–(20), after integration we obtain

$$\int_\Omega \big(\lambda \operatorname{div}(\mathbf{u}) - \alpha\, p\big)\operatorname{div}(\boldsymbol{\psi}) + 2\mu\,\mathcal{E}(\mathbf{u}) : \mathcal{E}(\boldsymbol{\psi})\,dxdy - \\ - \int_{\Gamma_f} (p + p_\infty + \mathbf{n}\cdot\boldsymbol{\tau}_0\langle\mathbf{n}\rangle + \sigma_{coh})\psi_2\,dx = 0, \tag{22}$$

$$\int\limits_{\Omega} S_\varepsilon \frac{\partial p}{\partial t}\varphi\, dxdy + \int\limits_{\Omega} \frac{k_r}{\eta_r}\nabla p\cdot\nabla\varphi\, dxdy + \int\limits_{\Omega} \alpha\,\frac{\partial}{\partial t}\Big(\operatorname{div}\mathbf{u}\Big)\varphi\, dxdy + \\ + \int\limits_{\Gamma_f} \frac{\partial v}{\partial t}\varphi\, dx + \int\limits_{\Gamma_f} \frac{v^3}{3\eta_f}\, p_x\varphi_x\, dx - Q(t)\varphi(0,0) = 0. \quad (23)$$

This formulation is not convenient on the computational use because of the necessity to track the fracture tips and change the size of Γ_f at every time step. Therefore, we modify Γ_f by regarding it as a potential fracture, which has closed part with $v = 0$ and the opened part with $v > 0$. However, under such interpretation the absence of the interpenetration of the opposite fracture walls in the computations cannot be guaranteed. In order to avoid this problem we impose the restriction

$$\Gamma_f: \quad v \geqslant 0, \quad (24)$$

by adding the penalty term

$$-\frac{1}{\delta}\int\limits_{\Gamma_f} \chi_{[v<0]}\, v\, \psi_2\, dx, \quad (25)$$

into the variational formulation. Here $\delta \ll 1$ is a small number, $\chi_{[v<0]}$ is the indicator function of set $\{\mathbf{x} : v(\mathbf{x}) < 0\}$.

The problem (23), (23) with (25) is solved using the finite element method via the open-source FEM package FreeFEM++ [14]. For the spatial discretization we use the piecewise-linear P1-elements over the triangulated computational domain Ω. The time derivatives are approximated with the first order of accuracy: $\dfrac{\partial f}{\partial t} \approx \dfrac{f^{n+1} - f^n}{\Delta t}$, where f denotes either of functions u, v or p; Δt is a time step. The upper index designates the number of the time step: $f^n = f(t^n, \mathbf{x})$, $t^n = t^0 + n\Delta t$. The computation starts with the intact state $\mathbf{u}^0 = 0$ and $p^0 = 0$ as the initial data. The non-linearity is resolved by the Newton-Raphson method.

4. Verification of the numerical algorithm

4.1. Convergence Test

In order to verify the algorithm we choose physical parameters typical for hydraulic fracturing problem and check the numerical convergence. For the verification the reservoir is assumed to be homogeneous. The reservoir is loaded by a uniform pre-stress caused by a far-field stress σ_∞:

$$\boldsymbol{\tau}_0\langle\mathbf{n}\rangle = -\sigma_\infty\mathbf{n}.$$

The following physical input parameters are used in simulations: domain size $R = 105$ m, maximal right tip position $L_r^{max} = 40$ m, maximal left tip position $L_r^{max} = 40$ m, Young's modulus $E = 17$ GPa, Poisson's ratio $\nu = 0.2$, energy release rate $G_c = 120$ Pa·m, critical cohesive stress $\sigma_c = 1.25$ MPa, initial porosity $\phi = 0.2$, reservoir permeability $k_r = 10^{-14}$ m^2, Biot coefficient $\alpha = 0.75$, storage coefficient $S_\varepsilon = 1.46 \times 10^{-11}$ Pa^{-1}, far-field stress $\sigma_\infty = 10$ MPa, reservoir pressure $p_\infty = 0$ MPa, reservoir fluid viscosity $\eta_r = 10^{-3}$ Pa·s, fracturing fluid viscosity $\eta_f = 10^{-1}$ Pa·s, injection rate per unit height $2\,Q = 10^{-3}$ m^2/s. Given Young's modulus E and Poisson's ratio ν, elasticity moduli λ and μ are calculated via the known formulas. The expression for the storage coefficient S_ε is given by formula (2).

Several simulations were conducted on the sequence of refining meshes. For the convergence test we compute the maximal relative difference in L_2-norm between solutions on two successive meshes:

$$\varepsilon_{max}(h) = \max\Big(\frac{||p_h - p_{h/2}||_{L_2}}{||p_h||_{L_2}}, \frac{||u_h - u_{h/2}||_{L_2}}{||u_h||_{L_2}}, \frac{||v_h - v_{h/2}||_{L_2}}{||v_h||_{L_2}}\Big) \times 100\% \quad (26)$$

The result of computations is demonstrated in Figure 5, where $h = \sqrt{S_{max}}$ is a mesh refining parameter and S_{max} is the maximal dimensionless area of all triangles in the corresponding mesh. One can see that at $h \approx 0.13$ the relative difference between solutions is less than 2 %. Therefore, this mesh was chosen for the further simulations.

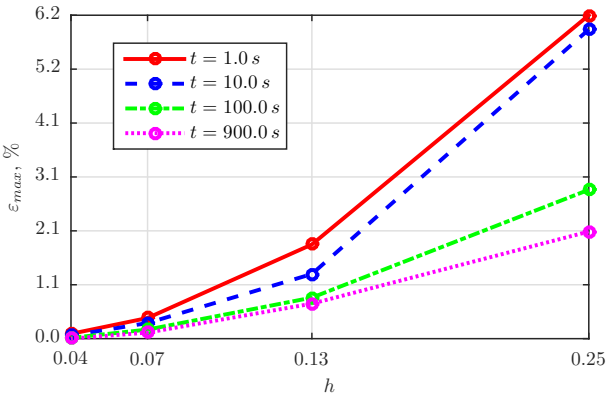

Figure 5. Relative difference in L_2-norm between solutions on two successive meshes for different time moments

4.2. Comparison with existing models

According to [15], [16], in the case of KGD-model the fracture propagation is governed by two competing energy dissipation mechanisms (viscous dissipation in fluid and creation of the new fracture surface) and two fluid storage mechanisms (in the fracture and in the reservoir). Therefore, there are four asymptotic regimes: storage-toughness dominated, leak-off-toughness dominated, storage-viscosity dominated and leak-off-viscosity dominated ones. All these regimes are demonstrated in paper [11] also in comparison with the analytical solution for KGD model. As a part of the model verification, we compare our results with the corresponding calculations of paper [11] in the case of the storage-toughness dominated regime.

The common input parameters used in simulations are the same as in Section 4.1, except for the domain size $R = 45$ m and maximal right and left tip positions $L_r^{max} = L_l^{max} = 15$ m. Also, we use equal viscosities for the reservoir and the fracturing fluids $\eta_r = \eta_f = 10^{-4}$ Pa·s to minimize the viscosity dissipation. Far-field stress is taken as $\sigma_\infty = 3.7$ MPa. Two simulations were carried out for permeabilities $k_r = 10^{-15}$ m^2 and $k_r = 10^{-16}$ m^2 during 14 s and 20 s, respectively, to ensure that the fracture propagates in the storage-toughness dominated regime. According to [11], for this set of parameters the results are in a good agreement with the early-time near-K solution [16] for the KGD model.

Good agreement of the fracture half-length in our model (solid lines 1, 2) and in [11] (marker lines 5, 6) is demonstrated in Figure 6. It confirms the consistency between the resulting fracture geometries and ones presented in [11]. A good match of the boundary of the cohesive zone (solid lines 3, 4 and marker lines 7, 8) indicates compliance in the implementation of the cohesive zone model.

5. Reservoir permeability contrast

In this Section, the model capabilities in the application to the hydraulic fracturing problem in the heterogeneous reservoir are demonstrated. The interesting case occurs when the reservoir

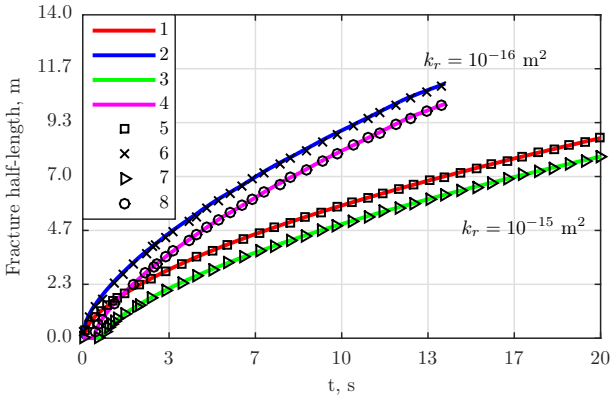

Figure 6. Fracture half-length in the is storage-toughness dominated regime: for $k_r = 10^{-15}$ m^2 (1) in present work, (5) in [11]; for $k_r = 10^{-16}$ m^2 (2) in present work, (6) in [11]. Position of the right boundary of the cohesive zone: for $k_r = 10^{-15}$ m^2 (3) in present work, (7) in [11]; for $k_r = 10^{-16}$ m^2 (4) in present work, (8) in [11].

has two layers (see Figure 7) with different permeabilities:

$$k_r(x) = \begin{cases} 10^{-14} \text{ m}^2, & x \leqslant x^*, \\ 10^{-16} \text{ m}^2, & x > x^*. \end{cases} \tag{27}$$

Here, $x = x^*$ denotes the border between layers, pictured as the brown line in Figure 7. Thus,

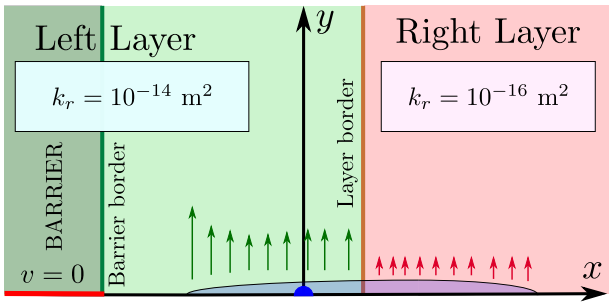

Figure 7. Reservoir with high-permeable (left) and low-permeable (right) layers. The barrier for fracture propagation is located in the high-permeable layer.

the leak-off from the fracture into the reservoir is higher in the left layer. The remaining simulation parameters are the same as in Section 4.1, except for the computational domain size parameters: $R = 150$ m, $L_\ell^{max} = 40$ m, $L_r^{max} = 73$ m. We propose the existence of a barrier located at $x = -L_\ell^{max}$ that prevents propagation of the fracture behind the barrier border.

The goal is to study the fracture dynamics depending on the location of the low-permeable layer relative to the injection point. Firstly, we place the layer border close to the wellbore at $x^* = 3.5$ m. Figure 8 (b) shows that the fracture reaches the layers border at $t \approx 35$ s and then proceeds its propagation further to the right. The leak-off in the low-permeable layer is lower; hence, the fracture becomes wider. The source of fluid at the wellbore near the border between the two layers supplies enough fluid to both sides of the fracture; therefore, the fracture propagates faster into the low-permeable layer where loss of fluid into the reservoir is lower (see Figure 8 (a)).

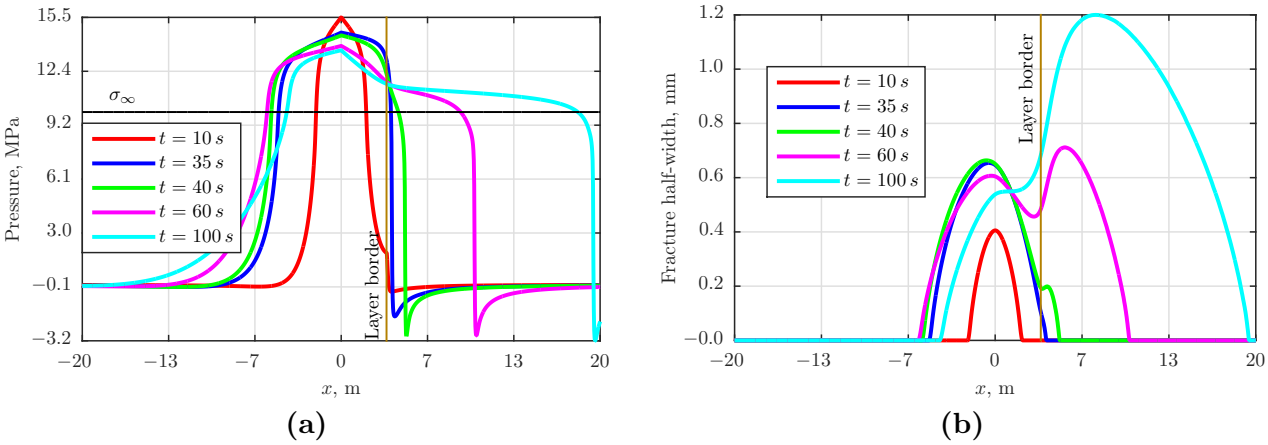

Figure 8. Pressure (a) and fracture half-width (b) along the fracture at different time for reservoir with two zones with high permeability contrast. The zones border (vertical brown line) is located at $x = 3.5$ m

The different situation occurs if we shift the border between the two layers with different permeabilities to $x^* = 10$ m (see Figure 9). The fracture propagates in both directions until the right tip enters the layer border. This occurs at $t \approx 200$ s and after that the fracture propagates to the left until the left fracture tip reaches the barrier at $t \approx 800$ s. For $200 \leq t \leq 800$ the pressure at the injection point stays almost at the constant level and, due to the lower permeability of the right layer, it becomes more difficult to increase the reservoir pressure for the further fracture growth to the right behind layer border. Thus, more fluid flows to the left half-wing of the fracture and only the left tip is moving. As the left tip reaches the barrier, it stops. As a result, the pressure starts growing over the whole fracture. When it overcomes some limit near the right layer border, the fracture breaks into the low-permeable layer and continues its propagation to the right direction.

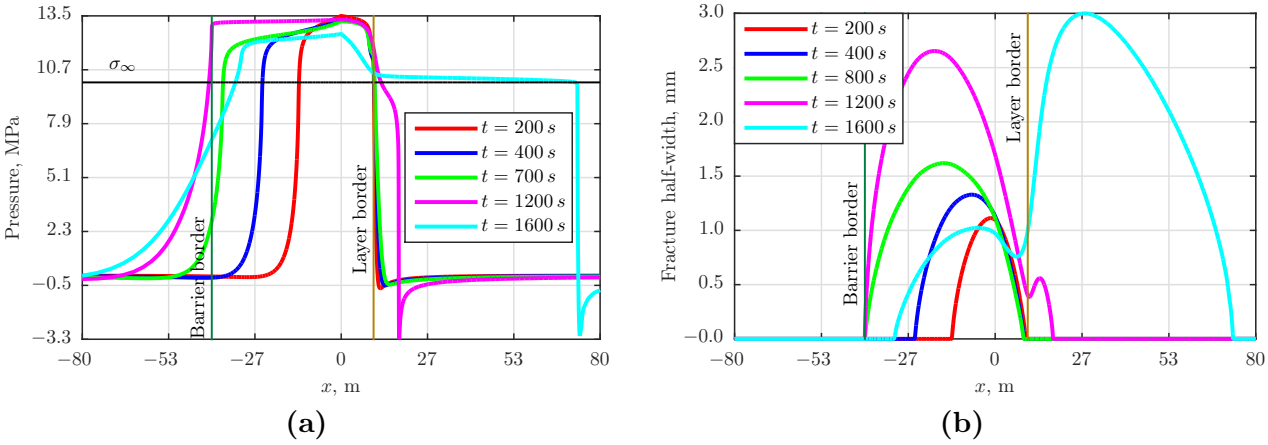

Figure 9. Pressure (a) and fracture half-width (b) along the fracture at different time for reservoir with two zones with high permeability contrast. The border between the permeability zones (vertical brown line) is located at $x = 10$ m

6. Conclusion

A numerical model of a hydraulic fracture propagating in a heterogeneous poroelastic medium is presented in the paper. The proposed approach accounts the influence of the pore fluid and the elastic rock deformation to the growth of the fracture. The fluid exchange between the reservoir and the fracture is naturally incorporated into the model. This makes it possible to state the complete problem in the single variational formulation with the mass conservation equation in the fracture playing the role of a natural nonlinear boundary condition. The cohesive zone model is used as a fracture propagation criterion.

The convergence of the numerical algorithm is checked by the comparison of the difference between solutions on the successively refining grids. Also, the simulation results are compared against the existing hydraulic fracture models, showing good agreement with numerical and analytical solutions.

The model capabilities are demonstrated on the case of reservoir with two layers with a permeability contrast. It is shown that fracture dynamics depends on the position of the border between the layers relative to the injection point. The fracture breaks into the low-permeable layer if the injection point is located near border between the layers. Otherwise, the fracture propagates through the high-permeable layer. The described non-stationary dynamics of the fracture grows demonstrates an importance of taking into account variability in physical properties of the reservoir for the correct modelling of the fracture development.

Acknowledgments

This work was supported by the RFBR grant (Project No. 16-01-00610).

References

[1] Adachi J, Siebrits E, Peirce A and Desroches J 2007 *Int. J. Rock Mech. and Min. Sci.* **44**(5) 739–57
[2] Detournay E 2016 *Ann. Rev. Fluid Mech* **48** 311–39
[3] Shelukhin V V, Baikov V A, Golovin S V, Davletbaev A Y and Starovoitov V N 2014 *International Journal of Solids and Structures* **51**(11) 2116–22
[4] Biot M A 1955 *Journal of Applied Physics* **26**(2) 182–5
[5] Biot M A 1956 *Journal of the Acoustical Society of America* **28**(2) 168–91
[6] Coussy O 2004 *Poromechanics* (John Wiley & Sons)
[7] Barenblatt G I 1962 *Adv Appl Mech* **7** 55–129
[8] Dugdale D 1962 *J Mech Phys* **8**(2) 100–4
[9] Geubelle P H and Baylor J S 1998 *Compos Part B* **29** 589–602
[10] Griffith A A 1921 *Philos T Roy Soc A* **221** 163–98
[11] Carrier B and Granet S 2012 *Engng Fract Mech* **79** 312–28
[12] Irwin G 1957 *J Appl Mech* **24** 361–4
[13] Economides M J and Nolte K G 2000 *Reservoir Stimulation* 3rd ed (John Wiley&Sons, LTD)
[14] Hecht F 2012 *J. Numer. Math.* **20** 251–65 ISSN 1570-2820
[15] Adachi J and Detournay E 2008 *Engng Fract Mech* **75**(16) 4666–94
[16] Bunger A, Detournay E and Garagash D 2005 *Int J Fract* **134**(2) 175–90